Near-isotropic 3D optical nanoscopy with photon-limited chromophores

Jianyong Tang[1], Jasper Akerboom, Alipasha Vaziri, Loren L. Looger, and Charles V. Shank[1]

Janelia Farm Research Campus, Howard Hughes Medical Institute, Ashburn, VA 20147

Imaging approaches based on single molecule localization break the diffraction barrier of conventional fluorescence microscopy, allowing for bioimaging with nanometer resolution. It remains a challenge, however, to precisely localize photon-limited single molecules in 3D. We have developed a new localization-based imaging technique achieving almost isotropic subdiffraction resolution in 3D. A tilted mirror is used to generate a side view in addition to the front view of activated single emitters, allowing their 3D localization to be precisely determined for superresolution imaging. Because both front and side views are in focus, this method is able to efficiently collect emitted photons. The technique is simple to implement on a commercial fluorescence microscope, and especially suitable for biological samples with photon-limited chromophores such as endogenously expressed photoactivatable fluorescent proteins. Moreover, this method is relatively resistant to optical aberration, as it requires only centroid determination for localization analysis. Here we demonstrate the application of this method to 3D imaging of bacterial protein distribution and neuron dendritic morphology with subdiffraction resolution.

3D bioimaging | nanoimaging | bacterial imaging | neuron imaging | biophotonics

Fluorescence microscopy allows the observation of biological samples in a highly sensitive, selective, and relatively noninvasive fashion. Moreover, fluorescence imaging tools can probe deeply into tissues to obtain volume images without physically isolating different sections. However, traditional fluorescence microscopy suffers from diffraction-limited resolution, far larger than actual molecular sizes. Recent development of two different superresolution (SR) fluorescence imaging methods has broken the diffraction limit and enables direct optical observation of biological features near molecular scales. One approach is to create a subdiffraction excitation pattern by stimulated emission depletion (1, 2) or structured illumination (3, 4), and the other approach is based on single molecule localization (5–9). An essential part of the single molecule localization methods involves centroid fitting of serial single molecule images at the detection plane in order to determine the lateral localization of each fluorescent molecule with precision limited not by diffraction, but mainly by its number of emitted photons. A superresolution 2D image of the sample can then be rendered by overlapping all single molecule localizations from all image frames. This principle of localization has also been applied to single particle tracking (10–14).

Single molecule-based superresolution microscopy requires individual chromophores to be turned "on" and "off" sequentially, either by photoswitching or by other stochastic photophysical processes. Compared to synthetic photoswitchable probes, photoactivatable fluorescent proteins (PA-FPs) (15–20) are superior in many regards: PA-FPs can be genetically fused to target proteins and endogenously expressed in cells and organelles, allowing live cell imaging; moreover, the genetic expression of the PA-FP ensures that it has nearly 100% specificity and efficiency of labeling target protein(s), a level impossible to reach by staining and conjugative probes; finally PA-FPs are much smaller than dye-labeled antibodies, permitting higher labeling density in biological

samples, allowing for higher imaging resolution according to the Nyquist criterion (21, 22).

However, each PA-FP molecule emits a limited number of photons (typically 200–1,000) (19, 23) before it bleaches (its "photon budget"), lower than typical synthetic dyes (>6,000) (24).

Recently, progress has been reported on extending single molecule-based SR techniques to three dimensions by generating axially sensitive defocusing patterns, such as astigmatism (25), dual-focal-plane imaging (26), and use of a double helical point spread function (PSF) (27) to resolve 3D localization of single emitters. In addition to these SR techniques, an interferometric approach (23) has been shown to be able to image biological samples labeled with fluorescent proteins (FPs) within a thickness on the order of the emission wavelength by ultrahigh axial resolution. However, each of these methods has limited biological applicability. Interferometric approaches are technically difficult to implement, and the limited axial range (on the order of the emission wavelength) impedes their application to thick biological samples. Defocusing methods require spreading photons over a larger spatial area at the detection plane, resulting in a much wider PSF. Under conditions of negligible background photon level and no pixelation noise, the single molecule localization uncertainty can be described as $\sigma = s/\sqrt{N}$, where s is the standard deviation of the PSF and N is the number of detected photons (28). According to this relationship, a wider PSF leads to a lower localization precision, unless a much higher number of photons is collected from each molecule. So it remains challenging to image samples of endogenously expressed FPs with limited photon budget by defocusing schemes. In addition, due to the intrinsic difference between the width of the lateral and axial PSFs of typical microscope objective lenses, axial resolution is at best two- to threefold worse than lateral resolution in defocusing schemes. Moreover, the defocusing patterns can be distorted by optical aberration when imaging deep regions. Experimental calibration of the PSF deviation is possible in some situations (29, 30), but remains difficult in heterogeneous samples such as brain tissue.

To overcome the challenges described above, we have developed a method, termed virtual volume superresolution microscopy (VVSRM), to map single fluorescent emitters in a virtual 3D space with near-isotropic 3D resolution. In this method, a tilted mirror is positioned near the sample region to generate a side view in addition to the front view. The side view provides axial information about the sample, enabling the precise determination of the 3D localization of single fluorescent molecules using centroid analysis in both the front and side views. Similar designs have been successfully implemented in 3D nano-

www.manaraa.com

metric particle tracking (31, 32) and in confocal microscopy to improve the axial resolution (33).

In this paper, we describe the experimental realization of VVSRM and demonstrate the application of this technique to superresolution imaging of bacterial cells and neuronal dendrites.

Results and Discussion

Experimental Realization of VVSRM. The principle of VVSRM is illustrated in Fig. 1. Built on an epifluorescence microscope coupled to an EMCCD camera, a microfabricated mirror on which the biological sample is mounted is placed near the focal plane of the microscope. The mirror is tilted at an angle θ with respect to the focal plane, to create a side view (virtual image), in addition to the front view (real image) of the fluorescent sample, and both are recorded simultaneously by the EMCCD camera. The spatial coordinates of the virtual image can be deduced by reflectional and rotational transformation of the front view coordinates:

$$x' = \cos(2\theta) \cdot x + \sin(2\theta) \cdot z, \qquad [1]$$

$$z' = \sin(2\theta) \cdot x - \cos(2\theta) \cdot z, \qquad [2]$$

$$y' = y, \qquad [3]$$

where (x',y',z') and (x,y,z) denote coordinates in virtual and real space, respectively (Fig. 1 *Inset*). When a single emitter is activated and excited, its fluorescence is projected to both views in a near-orthogonal fashion (one directly through the objective; the other from the mirror reflection), and its lateral and axial localizations can be simultaneously resolved. After serial activation, excitation, and localization of labeled fluorescent molecules, a 3D superresolution image can be computationally reconstructed, similar to other single molecule-based 2D SR imaging techniques. When $\theta = 45°$ ($x' = z$ and $z' = x$), the axial localization precision in the real image equals the lateral localization precision in the virtual image, enabling isotropic 3D resolution.

To observe real and virtual images in simultaneous focus, the fluorescence is split 50/50 to enable independent adjustment of each path. The 3D localization of single fluorescent molecules can thus be determined with the optimal PSF. We tested the 3D localization precision of single fluorescence beads (diameter
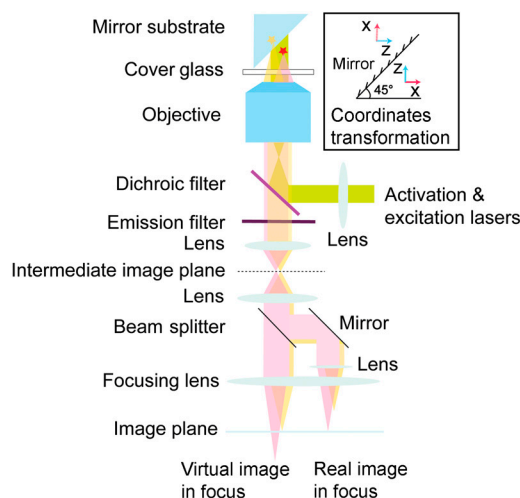
Fig. 1. VVSRM principle and experimental realization. Pink and yellow colors denote the fluorescence paths of real and virtual images, respectively. A 50/50 beam splitter was used to allow independent focusing of both real and virtual images. The inset illustrates how the spatial coordinates of a single emitter in the real image are transformed by rotation and reflection in the tilted mirror into a virtual image.
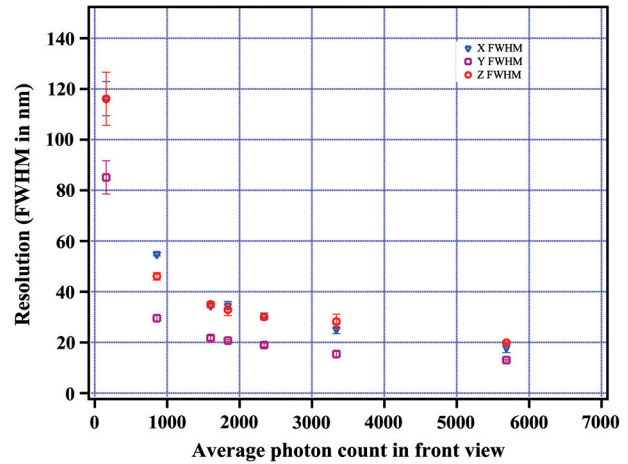

Fig. 2. A 3D-imaging resolution of VVSRM as a function of photon counts from the front view. A 40-nm fluorescent bead was used as point emission source, and the fluorescence intensity was modulated by excitation laser intensity. In this experiment, the mirror tilt angle was 54.7° (from a silicon V groove). The error bars represent the standard error of the localization distribution width in the fitting procedure.

of 40 nm) with a typical experimental setting (54.7° tilt angle), and the results are presented in Fig. 2. There are several possible factors contributing to the slight differences in the localization precision in X, Y, and Z, including the tilt angle (optimal isotropy at 45°) and the reflection efficiency of the mirror coating. Under conditions with photon budgets of ~500 (comparable to that of most fluorescent proteins, and taking into account the photon loss due to fluorescence splitting), this technique enables sub-100-nm localization precision in all three dimensions. For bright dye molecules with photon budgets over ~5,000, this method should achieve sub-20-nm isotropic 3D resolution.

Imaging Bacteria by VVSRM. To demonstrate the potential of this superresolution microscopy technique, we present the virtual volume subdiffraction imaging of protein assembly and distribution in single fixed *Escherichia coli* cells, in which a target protein is fused to mEos2, a green-to-red photoactivatable fluorescent protein (19).

The first protein we used in our study is the CRISPR (clustered regularly interspaced short palindromic repeats)-associated protein Cas2, a protein involved in phage resistance in bacteria and archaea (34). Cas2 is present in wild-type *E. coli* K12 strains, but absent in *E. coli* BL21(DE3), making it an ideal candidate for analysis. A recent report on distant homologues of the *E. coli* Cas2 proteins from six different organisms suggests that the Cas2 proteins are endoribonucleases specific for single-stranded RNAs, preferentially cleaving within U-rich regions (35); the activity of the *E. coli* Cas2 protein has not been confirmed. As shown in Fig. 3, overexpressed mEos2-tagged Cas2 proteins accumulated tightly near both poles of *E. coli* BL21(DE3) cells. It has been shown that bacteriophage infection takes place preferentially at the poles of bacterial cells (36). The tight localization of Cas2 at the poles of the *E. coli* cells is in good agreement with the preferred point of bacteriophage entry; thus it is tempting to speculate that Cas2 localization plays a role in phage resistance. It has recently been reported that protein aggregates can also be accumulated at the poles of bacterial cells (37), so further analysis is needed to prove the in vivo relevance of this observed localization of overexpressed Cas2. Single molecules with localization precision (FWHM) worse than 100 nm are filtered out in data analysis. The 3D image of the two polar Cas2 protein assemblies generated by VVSRM allows accurate measurement of their volumes, which are 0.078 fL and 0.088 fL, respectively, in total occupying about 10–20% of the *E. coli* cell volume (38).

Tang et al.
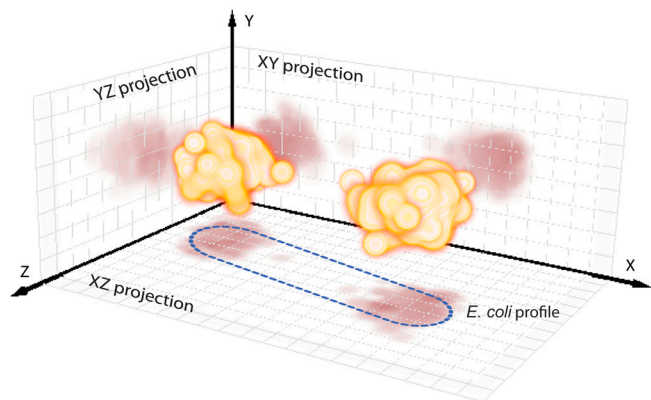
Fig. 3. A 3D-VVSRM 3D image of Cas2-mEos2 in a single *E. coli* cell and its projections (dark) onto three perpendicular planes. The blue dashed line outlines the profile of the *E. coli* cell. Grid separation: 250 nm. The cultured bacterial cells were attached to an Al/SiO₂-coated silicon V-groove surface by poly-L-lysine and fixed by 4% paraformaldehyde in PBS buffer. See Movie S1.

If rendered with the resolution of confocal microscopy, their computed volumes are 1.45 fL and 1.55 fL, respectively, much bigger than the cell itself. The results show the capability of VVSRM to image FP-labeled biological samples with sub-100-nm 3D resolution and dramatically improve the accuracy of volume measurements. VVSRM provides a tool to directly image the 3D internal structure of bacteria and archaea, the sizes of which are generally near or below the resolution limit of traditional optical microscopy.

We also measured the spatial distribution of the bacterial actin homologue, MreB, in *E. coli* cells. MreB forms helix-like structures encircling rod-shape bacterial cells (39). Emerging evidence suggests that MreB plays a critical role in a wide range of essential bacterial cellular functions (9, 39–47) such as cell division, chromosome segregation, cell shape, and polarity. Quantitative single molecule measurements of tagged MreB in the bacterium *Caulobacter crescentus* (42) indicated the presence of both polymerized and unpolymerized populations of MreB: The polymerized MreB molecules undergo directional movements, whereas unpolymerized MreB molecules are thought to primarily associate with the cell membrane. In our experiment, the gene encoding

mEos2 was fused to the N terminus of *E. coli* MreB via a small linker, cloned into the pRSF-1 expression vector and overexpressed in wild-type *E. coli* K12 W3110 containing the lambda DE3 lysogen [K12(DE3)]. As shown in Fig. 4, mEos2-tagged MreB distributed close to the cell membrane, leaving the cytoplasm empty. We did not observe a helical or ring distribution of MreB molecules as described earlier (48–50). This might be attributed to the presence of abundant overexpressed MreB molecules. Despite difficulties in interpreting the localization of polymerized MreB, our results are consistent with the suggestion that unpolymerized MreB molecules associate with the inner membrane of the bacterial cell.

As the width of *E. coli* K12(DE3) cells is about 500 nm, it is impossible to fully resolve the 3D arrangement we observed by using conventional light microscopy methods such as confocal microscopy. This result further demonstrates the capacity of VVSRM to resolve subdiffraction cellular localization and structure in bioimaging.

As demonstrated in these examples, VVSRM enables 3D imaging or tracking of structural and functional proteins near or at the molecular scale. VVSRM is a useful tool for dissecting cellular and subcellular fine structures that would be difficult or impossible to resolve by conventional microscopy, especially in small-cell organisms such as bacteria. Moreover, the current VVSRM setup allows for multicolor imaging, so it will be possible to probe the colocalization of different protein components tagged with distinct photoactivatable fluorescent proteins, enabling the elucidation of protein-protein interactions with molecular scale resolution.

Neuronal Imaging by VVSRM. In addition to the localization analysis of Cas2 and MreB in *E. coli* cells, we demonstrate the potential of VVSRM in imaging a neuronal dendrite with superresolution in Fig. 5. We incorporate the points accumulation for imaging in nanoscale topography (PAINT) technique (8), using the environmentally sensitive dye Nile Red, which becomes fluorescent only when it transiently binds to cellular membranes. This diffusion-controlled process also enables the stochastic and serial activation of single emitters for superresolution imaging. It is possible with the PAINT technique to image any membrane structure with high percentage coverage even with low probe concentration (<1 nM), due to the small dye size and almost unlimited mole-

A   B
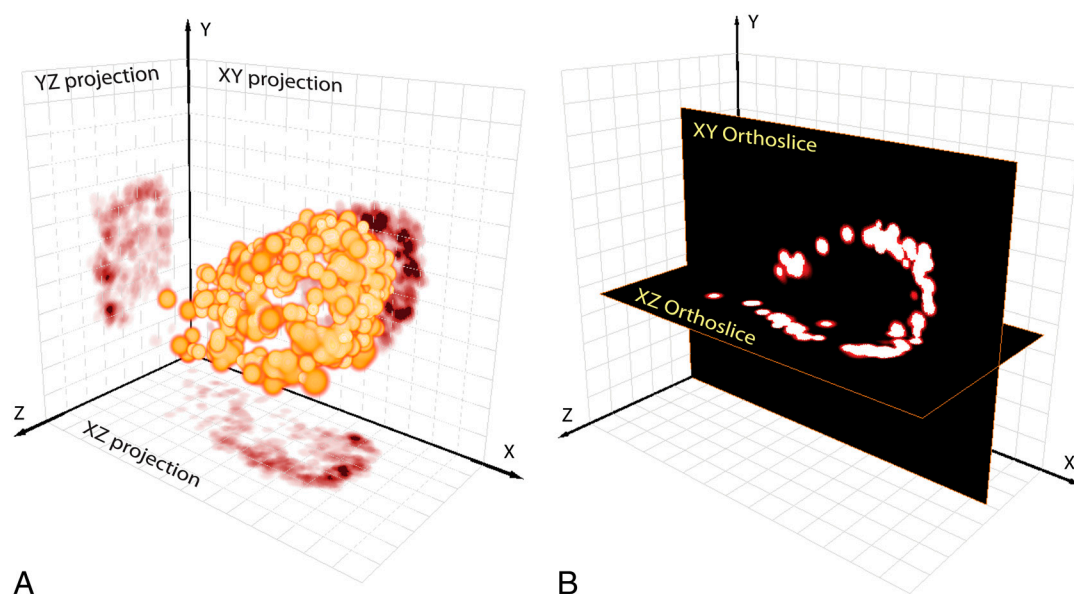
Fig. 4. A 3D-superresolution VVSRM image (*A*) with projection onto XY, YZ, and XZ planes and intersectional PALM image (*B*) of MreB tagged with the photoactivatable fluorescent protein mEos2 in an *E. coli* cell. Grid separation: 250 nm. The cultured bacterial cells were attached to an Al/SiO₂-coated coverslip glass surface by poly-L-lysine and fixed by 4% paraformaldehyde in PBS buffer. See Movie S2.
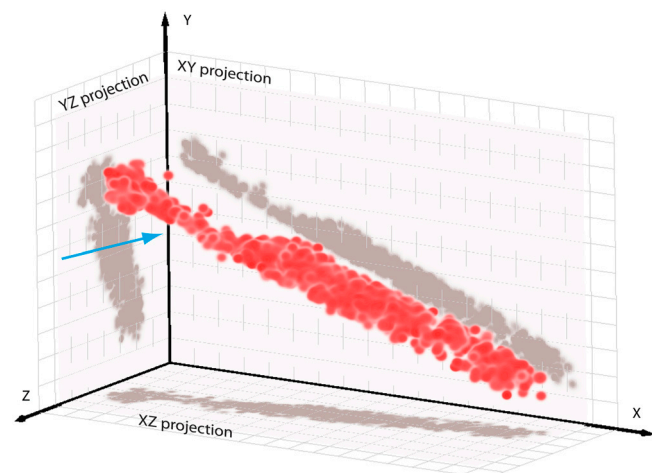
Tang et al.

cular sampling. Because the number of photons collected from each probe molecule in PAINT is limited by the membrane-bound dwell time, photon-efficient VVSRM is suitable to combine with PAINT to extract the 3D subdiffraction membrane profile. The setup was almost identical to the one for bacterial imaging, except that a 30° tilted gold-coated mirror was used to create the virtual image, and molecules with localization precision (FWHM) better than 150 nm were selected.

The results in Fig. 5 show that VVSRM is well suited to probe the 3D structure of neuronal dendrites in fine detail. Structural features such as the dendritic invagination (51) (indicated by the blue arrow in Fig. 5, the dendritic diameter shrinks to about 200 nm from 600 nm) would have been difficult to resolve in conventional 3D imaging. VVSRM will be useful for fine mapping of neuronal morphology and other complex small-scale 3D anatomical structures for projects such as the reconstruction of neurons and neural circuits. Future experiments might entail visualization of small features such as dendritic spines, membrane protein mapping along branched neurons, and small volume calculations of protein abundance.

Discussion

The proof-of-principle experiments described above reveal some key features of the VVSRM imaging approach. Due to the reflectional and rotational transformation process, the field of view of VVSRM is currently limited by the depth-of-focus range of the microscope in both X and Z dimensions. The examples described, bacterial cells and dendrites, are ideal biological systems to be imaged by VVSRM, because they can be easily aligned within the field of view, avoiding overlap between the real and virtual images. To image a sample with a size beyond this scale, multiple regions can be subsequently imaged and tiled in order to construct a volume SR image of the whole sample, using an illumination pattern that confines the excitation and/or activation regions in the X and Z directions. Potentially, a strip-like illumination pattern can be generated by nonlinear optical sectioning methods such as temporal focusing (52), and images of much larger volumes can be reconstructed by tiling these strip-shaped 3D subimages generated at different stage positions.

VVSRM improves 3D resolution mostly because the tilted mirror helps to capture more photons (nearly a factor of 2) and effectively expands the fluorescence collection angle at least along one dimension. The experimental results indicate that this gain in resolution can even compensate for the loss in photon efficiency due to 50/50 beam splitting. Moreover, future improvements will include replacing the beam splitter with a sharp-edged mirror placed at the intermediate image plane (Fig. 1), so that the localization precision in both real and virtual images can be improved by a factor of $\sqrt{2}$.

There are three major advantages of VVSRM over other 3D SR imaging techniques. First, it requires a smaller photon budget than defocusing techniques, since single-emitter localizations along all directions are obtained from in-focus images. This enables imaging of weak FP-labeled biological samples with almost isotropic sub-100-nm resolution. Usage of larger photon-budget chromophores and more efficient photon detection will result in higher temporal resolution of SR imaging. In addition, the focused single molecule images allow a high density of fluorescent molecules to be activated in each cycle.

Second, VVSRM is less vulnerable than other 3D SR techniques to undesirable optical aberration and axial drift of the sample stage, because only lateral centroid localizations of single emitters in the real and virtual images are needed. Thus it is possible to probe deeply into biological tissues with higher resolution and less aberration. However, in highly heterogeneous and aberrating samples, serious localization errors can still occur even with centroid fitting. Caution should be taken when VVSRM is extended to larger scales, even though the relative localization of single molecules within a small volume should be less affected by such errors than in larger volumes. In addition, certain combinations of mirror angle and objective numerical aperture can lead to significant, intrinsic localization errors (53).

Third, VVSRM is very simple to implement on a conventional fluorescence microscope, providing a low technical barrier for biological applications. In brief, VVSRM is uniquely suited to resolve weak chromophores in thick samples with near-isotropic 3D superresolution and is complementary to current SR imaging tools.

Materials and Methods

Mirror Substrate Preparation and Configuration. For *E. coli* imaging, two types of substrates were used. Silicon V grooves (O/E Land Inc., with tilted angle of 54.7°) or flat microscope glass coverslips were sequentially coated with a 150-nm layer of aluminum and 0.7- or 1.4-μm layer of silicon dioxide (Thin Film Coating LLC). Before use, the coated substrates were washed with deionized water and treated in UV/Ozone (BioForce Inc.) for 20 min. The tilted angle of the metal coated coverslip was adjusted to 45°. Though a 45°-tilted angle is optimal for simple and precise determination of axial location of single emitters according to formula **1**, in practice the silicon V groove (with angle = 54.7° due to its crystal structure) has the advantage of a clear edge, which is preferable for high numerical aperture objectives with small working distance. In the case of cultured neuron imaging, the aluminum coating did not survive long-term incubation (1 to 2 weeks) in growth medium, so a commercial gold-coated mirror (Thorlabs) was used, and the tilted angle was set to 30° to allow a view of a larger area of the mirror surface away from the mirror edge, making it easier to find dendrites.

Gene Cloning, Transformation And Expression for *E. coli* VVSRM Imaging. The gene encoding Cas2 was PCR-amplified from *E. coli* (K12 W3110) genomic DNA with primers 5′- CCCGGG<u>TCATGA</u>GTATGTTGGTCGTGGTC-3′ and 5′-CCCGGG<u>GCGGCCGC</u>TAACAGGTAAAAAAGACACCAACC-3′ (BspHI and NotI sites underlined), digested, and cloned into predigested pRSF-1 (EMD Biosciences). *meos2* was PCR-amplified from pRSETA-*meos2* with primers 5′-GGGCCC<u>GCGGCCGC</u>GGCAGCGGCATGAGTGCGATTAAGCCAGAC-3′ and 5′-CCCGGG<u>CCTAGG</u>TTATCGTCTGGCATTGTCAGG-3′ (NotI and AvrII sites underlined), digested, and cloned into predigested pRSF-1 containing *cas2*. The resulting construct containing *cas2-meos2* fused with the linker Ser-Gly-Arg-Gly-Ser-Gly was verified by sequence analysis. *E. coli* XL-1 (Stratagene) was used during cloning.

E. coli BL21(DE3) (EMD Biosciences) was used as a bacterial host for expression of Cas2-mEos2. Cells were transformed by heat shock, and successful transformants were selected and grown in a 100-mL 2-YT medium at 37 °C in a rotary shaker until the optical density at 600 nm (OD$_{600}$) reached 0.5. Isopropyl-β-D-thiogalactopyranoside was then added to a final concentration of 1 mM. The culture was incubated for an hour at 37 °C in a rotary shaker. Cells were harvested by centrifugation (2,000 × g, 4 °C) and

Fig. 5. A 3D-VVPAINT imaging of a rat hippocampal neuronal dendrite, one week after isolation and culturing. Grid separation: 500 nm. Cultured neurons were attached to the gold mirror surface by Matrigel, incubated in growth medium, and later fixed by 4% paraformaldehyde in PBS buffer. The arrow points to an invagination of the dendrite. See Movie S3.

Tang et al.

resuspended in 5 mL PBS, and stored on ice. Before imaging, the bacterial cells were fixed on the substrate surface with 4% paraformaldehyde in PBS buffer.

The gene encoding MreB was PCR-amplified from *E. coli* K12 (W3110) genomic DNA with primers 5′-ATGCCAGACGAGAATTCGAGCTCTTGAAAAA-ATTTCGTGGCATG-3′ and 5′- GGGCCC**CTCGAG**TTACTCTTCGCTGAACAGGTC-3′ (XhoI site underlined), *meos2* was PCR-amplified from pRSETA-*meos2* with primers 5′-GGCGG**CCATGG**GTAGTGCGATTAAGCCAGACATG-3′ and 5′- ATTT-TTTCAAGAGCTCGAATTCTCGTCTGGCATTGTCAGGC-3′ (NcoI site underlined). The resulting overlapping PCR products were gel-purified, assembled by assembly PCR, digested with XhoI/NcoI, and ligated into predigested pRSF-1 (EMD Biosciences). The resulting construct containing *meos2-mreb* fused with the linker Glu-Phe-Glu-<u>Leu</u> (the first methionine of MreB was replaced by a leucine, underlined) was verified by sequence analysis. *E. coli* XL-1 (Stratagene) was used for cloning. The *E. coli* K12 (W3110) λDE3 lysogen [*E. coli* K12(DE3)] was constructed using the λDE3 Lysogenization Kit from Novagen following the manufacturer's instructions and used as a bacterial host for expression of mEos2-MreB. Transformation and expression of mEos2-MreB was the same as for Cas2-mEos2, only for mEos2-MreB *E. coli* K12(DE3) was used as a host for expression.

Rat Neuron Sample Preparation for VVSRM Imaging. Primary hippocampal neurons were isolated from the hippocampus of P1 pups of Sprague Dawley rats, and the neurons were dissociated by papain (Worthington) digestion and plated on mirror substrate coated with Matrigel (Collaborative Biochemical Product, Inc.) diluted 1:50 in MEM (Invitrogen). Neurons were initially maintained in the plating medium, which is MEM supplemented with 0.02% NaHCO₃, 0.5% glucose, 0.01% transferrin (Calbiochem), FBS (HyClone, 10 mL per 100-mL medium), L-glutamine (GIBCO, 1 mL 0.2 M solution per 100-mL medium), and insulin (Sigma, 2.5 mg per 100-mL medium). After 24 h, the plating medium was removed and the growth medium was applied to the cells. The growth medium is MEM supplemented with 0.02% NaHCO₃, 0.5% glucose, 0.01% transferrin, FBS (5 mL per 100-mL medium), L-glutamine (0.25 mL 0.2 M solution per 100-mL medium), and B-27 (GIBCO, 2 mL per 100-mL medium). In some experiments cytosine arabinoside (cytarabine; Sigma, 4 μM) was added after several days to minimize growth of nonneuronal cells. After 1 or 2 weeks of growth, the neurons were rinsed briefly with PBS and fixed with 4% paraformaldehyde in 0.1-M phosphate buffer (pH 7.4) for 10 min. To find dendrites to image, the neurons were immunologically stained with an antibody labeled with green fluorescent dye (Alexa 488), which can be optically separated from the red fluorescence of Nile Red. In the staining procedure, the neurons were blocked and permeabilized with 5% normal goat serum, 0.1% Triton X-100 (Sigma) in PBS (pH 7.4). The primary antibody (rabbit polyclonal neuron specific beta III tubulin, Abcam Inc.) was diluted to a concentration of 1 μg/mL in 5% normal goat serum and 0.1% Triton X-100 in PBS, applied to cells and allowed to incubate overnight at 4 °C. The secondary antibody (Alexa Fluor 488, goat anti-rabbit IgG, Invitrogen) was diluted to a concentration of 4 μg/mL in 5% normal goat serum and 0.1% Triton X-100 in PBS and applied to cells and incubated for 2 h at room temperature before imaging. The Alexa Fluor 488-labeled neurons and neuronal features were located by epifluorescence imaging (excited by a xenon lamp filtered by blue filters: 472/30 nm, Semrock Inc.), collected through green filters (525/30 nm, Semrock Inc.), and subsequently imaged by VVSRM on the same microscope. During imaging, the gold mirror with the fixed neuron sample was immersed in Nile Red (Sigma, 1 nM in PBS buffer) solution.

VVSRM Microscope Setup. In the experimental setup of VVPALM imaging, both the activation laser (405 nm, 50 mW, CUBE, Coherent Inc.) and the excitation laser (561 nm, 25 mW, DPSS laser, Crystal Laser) were collinearly coupled into an inverted fluorescence microscope (Olympus, IX71) with an objective (Olympus 60X, NA 1.2, water immersion). A dichroic mirror (XF2043, Omega Optics Inc.) was used to separate the fluorescence emission signal from laser reflection and scattering. The polarization of the excitation laser was arranged to be parallel to the tilted mirror plane. An achromatic lens ($f = 500$ mm) was used to focus the laser beams onto the back focal plane of the objective, in order to construct an epifluorescence scheme. The fluorescence beam was further purified with a triple-band notch filter (405/488/561 nm, Semrock, Inc.) and emission filters (617/75 nm, Semrock Inc.). A homebuilt fluorescence detection setup was initially used: The fluorescence from the real and virtual views was separated by a nonpolarizing 50/50 beam splitter, independently relayed with 1.5× magnification, and focused onto different regions of the same EMCCD camera (Andor Technology, iXon+, DU888, 1,024 by 1,024 pixels) by a prism mirror (Edmund Optics). Alternatively, a Quad-View system (Photometrics, with built-in customized beam splitter) coupled with a 1.6× magnifier was used for the same purpose. Solis image acquisition software (Andor Technology) was used for data collection.

The power of the excitation laser was attenuated by neutral density (ND) filters (Thorlabs Inc.) to 2–6 mW before entering the objective. The exposure time for each frame was 20–100 ms. The intensity of the activation laser was modulated by a motorized ND filter wheel (Thorlabs Inc.), such that the photoactivated fluorescent protein molecules were serially activated with intensity optimal for spatial separation of single fluorescent molecules.

For neuronal imaging, the same setup was used, with the following modifications: Only the excitation laser ($\lambda = 561$ nm) was used (the activation laser was not needed for Nile Red); furthermore, a dipping objective lens (Olympus, 60X, NA1.1, working distance 1.5 mm) was implemented to visualize a larger area on the mirror. The mirror surface was immersed in a 1-nM solution of Nile Red (Sigma) in PBS for PAINT-type imaging.

Image Processing. As a first step, the stack of fluorescence images recorded with the Andor EMCCD camera was analyzed by the Peakselector software package (23) in order to obtain 2D single molecule localization in both real and virtual images. The algorithm is described in Betzig et al. (5). Second, an algorithm to match molecules in the real and virtual images was applied in the Matlab software suite (Mathworks Inc.) to render a 3D volume SR image. The criteria for matching are based on the observation that the same single molecule should appear in both real and virtual images at the same time and same Y location within experimental uncertainty. Finally, the volume image was presented in Amira (Visage Imaging Inc.). To calculate the volume of a protein assembly, the 3D virtual space was partitioned into cubic units (10 nm × 10 nm × 10 nm), a length scale that should be set to be much smaller than the imaging resolution. Then the summation of all the units with fluorescence intensity above a threshold (half of the average single molecule peak intensity) resulted in the estimated protein volume.

1. Hell SW, Wichmann J (1994) Breaking the diffraction resolution limit by stimulated-emission—stimulated-emission-depletion fluorescence microscopy. *Opt Lett* 19(11):780–782.

2. Hein B, Willig KI, Hell SW (2008) Stimulated emission depletion (STED) nanoscopy of a fluorescent protein-labeled organelle inside a living cell. *Proc Natl Acad Sci USA* 105:14271–14276.

3. Gustafsson MGL (2000) Surpassing the lateral resolution limit by a factor of two using structured illumination microscopy. *J Microsc-Oxford* 198:82–87.

4. Gustafsson MGL (2005) Nonlinear structured-illumination microscopy: Wide-field fluorescence imaging with theoretically unlimited resolution. *Proc Natl Acad Sci USA* 102:13081–13086.

5. Betzig E, et al. (2006) Imaging intracellular fluorescent proteins at nanometer resolution. *Science* 313:1642–1645.

6. Hess ST, Girirajan TPK, Mason MD (2006) Ultra-high resolution imaging by fluorescence photoactivation localization microscopy. *Biophys J* 91:4258–4272.

7. Rust MJ, Bates M, Zhuang XW (2006) Sub-diffraction-limit imaging by stochastic optical reconstruction microscopy (STORM). *Nat Methods* 3:793–795.

8. Sharonov A, Hochstrasser RM (2006) Wide-field subdiffraction imaging by accumulated binding of diffusing probes. *Proc Natl Acad Sci USA* 103:18911–18916.

9. Biteen JS, et al. (2008) Super-resolution imaging in live Caulobacter crescentus cells using photoswitchable EYFP. *Nat Methods* 5:947–949.

10. Gelles J, Schnapp BJ, Sheetz MP (1988) Tracking kinesin-driven movements with nanometre-scale precision. *Nature* 331:450–453.

11. Kao HP, Verkman AS (1994) Tracking of single fluorescent particles in 3 dimensions—use of cylindrical optics to encode particle position. *Biophys J* 67:1291–1300.

12. Pavani SRP, Piestun R (2008) Three dimensional tracking of fluorescent microparticles using a photon-limited double-helix response system. *Opt Express* 16:22048–22057.

13. Toprak E, Balci H, Blehm BH, Selvin PR (2007) Three-dimensional particle tracking via bifocal imaging. *Nano Lett* 7:2043–2045.

Tang et al.

14. Yildiz A, et al. (2003) Myosin V walks hand-over-hand: Single fluorophore imaging with 1.5-nm localization. *Science* 300:2061–2065.
15. Lippincott-Schwartz J, Patterson GH (2003) Development and use of fluorescent protein markers in living cells. *Science* 300:87–91.
16. Patterson GH, Lippincott-Schwartz J (2002) A photoactivatable GFP for selective photolabeling of proteins and cells. *Science* 297:1873–1877.
17. Ando R, Hama H, Yamamoto-Hino M, Mizuno H, Miyawaki A (2002) An optical marker based on the UV-induced green-to-red photoconversion of a fluorescent protein. *Proc Natl Acad Sci USA* 99:12651–12656.
18. Chudakov DM, et al. (2004) Photoswitchable cyan fluorescent protein for protein tracking. *Nat Biotechnol* 22:1435–1439.
19. McKinney SA, Murphy CS, Hazelwood KL, Davidson MW, Looger LL (2009) A bright and photostable photoconvertible fluorescent protein. *Nat Methods* 6:131–133.
20. Subach FV, et al. (2009) Photoactivatable mCherry for high-resolution two-color fluorescence microscopy. *Nat Methods* 6:153–159.
21. Shannon CE (1949) Communication in the presence of noise. *Proc Inst Radio Eng* 37:10–21.
22. Shroff H, Galbraith CG, Galbraith JA, Betzig E (2008) Live-cell photoactivated localization microscopy of nanoscale adhesion dynamics. *Nat Methods* 5:417–423.
23. Shtengel G, et al. (2009) Interferometric fluorescent super-resolution microscopy resolves 3D cellular ultrastructure. *Proc Natl Acad Sci USA* 106:3125–3130.
24. Bates M, Huang B, Dempsey GT, Zhuang XW (2007) Multicolor super-resolution imaging with photo-switchable fluorescent probes. *Science* 317:1749–1753.
25. Huang B, Wang WQ, Bates M, Zhuang XW (2008) Three-dimensional super-resolution imaging by stochastic optical reconstruction microscopy. *Science* 319:810–813.
26. Juette MF, et al. (2008) Three-dimensional sub-100 nm resolution fluorescence microscopy of thick samples. *Nat Methods* 5:527–529.
27. Pavani SRP, et al. (2009) Three-dimensional, single-molecule fluorescence imaging beyond the diffraction limit by using a double-helix point spread function. *Proc Natl Acad Sci USA* 106:2995–2999.
28. Thompson RE, Larson DR, Webb WW (2002) Precise nanometer localization analysis for individual fluorescent probes. *Biophys J* 82:2775–2783.
29. Deng Y, Shaevitz JW (2009) Effect of aberration on height calibration in three-dimensional localization-based microscopy and particle tracking. *Appl Optics* 48:1886–1890.
30. Mlodzianoski MJ, Juette MF, Beane GL, Bewersdorf J (2009) Experimental characterization of 3D localization techniques for particle-tracking and super-resolution microscopy. *Opt Express* 17:8264–8277.
31. McMahon MD, Berglund AJ, Carmichael P, McClelland JJ, Liddle JA (2009) 3D particle trajectories observed by orthogonal tracking microscopy. *ACS Nano* 3:609–614.
32. Seale KT, et al. (2008) Mirrored pyramidal wells for simultaneous multiple vantage point microscopy. *J Microsc-Oxford* 232:1–6.
33. Lindek S, Stefany T, Stelzer EHK (1997) Single-lens theta microscopy—a new implementation of confocal theta microscopy. *J Microsc-Oxf* 188:280–284.
34. Brouns SJJ, et al. (2008) Small CRISPR RNAs guide antiviral defense in prokaryotes. *Science* 321:960–964.
35. Beloglazova N, et al. (2008) A novel family of sequence-specific endoribonucleases associated with the clustered regularly interspaced short palindromic repeats. *J Biol Chem* 283:20361–20371.
36. Edgar R, et al. (2008) Bacteriophage infection is targeted to cellular poles. *Mol Microbiol* 68:1107–1116.
37. Rokney A, et al. (2009) E. coli transports Aggregated Proteins to the Poles by a Specific and Energy-Dependent Process. *J Mol Biol* 392:589–601.
38. Kubitschek HE (1990) Cell volume increase in Escherichia coli after shifts to richer media. *J Bacteriol* 172:94–101.
39. Shih YL, Rothfield L (2006) The bacterial cytoskeleton. *Microbiol Mol Biol R* 70:729–754.
40. Figge RM, Divakaruni AV, Gober JW (2004) MreB, the cell shape-determining bacterial actin homologue, co-ordinates cell wall morphogenesis in Caulobacter crescentus. *Mol Microbiol* 51:1321–1332.
41. Gitai Z, Dye N, Shapiro L (2004) An actin-like gene can determine cell polarity in bacteria. *Proc Natl Acad Sci USA* 101:8643–8648.
42. Kim SY, Gitai Z, Kinkhabwala A, Shapiro L, Moerner WE (2006) Single molecules of the bacterial actin MreB undergo directed treadmilling motion in Caulobacter crescentus. *Proc Natl Acad Sci USA* 103:10929–10934.
43. Kruse T, Gerdes K (2005) Bacterial DNA segregation by the actin-like MreB protein. *Trends Cell Biol* 15:343–345.
44. Madabhushi R, Marians KJ (2009) Actin Homolog MreB Affects Chromosome Segregation by Regulating Topoisomerase IV in Escherichia coli. *Mol Cell* 33:171–180.
45. Munoz-Espin D, et al. (2009) The actin-like MreB cytoskeleton organizes viral DNA replication in bacteria. *Proc Natl Acad Sci USA* 106:13347–13352.
46. Shih YL, Kawagishi I, Rothfield L (2005) The MreB and Min cytoskeletal-like systems play independent roles in prokaryotic polar differentiation. *Mol Microbiol* 58:917–928.
47. Varma A, Young KD (2009) In Escherichia coli, MreB and FtsZ direct the synthesis of lateral cell wall via independent pathways that require PBP 2. *J Bacteriol* 191:3526–3533.
48. Espeli O, Nurse P, Levine C, Lee C, Marians KJ (2003) SetB: An integral membrane protein that affects chromosome segregation in Escherichia coli. *Mol Microbiol* 50:495–509.
49. Jones LJF, Carballido-Lopez R, Errington J (2001) Control of cell shape in bacteria: Helical, actin-like filaments in Bacillus subtilis. *Cell* 104:913–922.
50. Shiomi D, Yoshimoto M, Homma M, Kawagishi I (2006) Helical distribution of the bacterial chemoreceptor via colocalization with the Sec protein translocation machinery. *Mol Microbiol* 60:894–906.
51. Bhide PG, Lieberman AR, Campbell G (1988) Dendritic invagination of developing optic tract axons in the hamster. *Exp Brain Res* 73:519–522.
52. Vaziri A, Tang JY, Shroff H, Shank CV (2008) Multilayer three-dimensional super resolution imaging of thick biological samples. *Proc Natl Acad Sci USA* 105:20221–20226.
53. Berglund AJ, McMahon MD, McClelland JJ, Liddle JA (2010) Theoretical model of errors in micromirror-based three-dimensional particle tracking. *Opt Lett*, in press.

BIOPHYSICS AND COMPUTATIONAL BIOLOGY

APPLIED PHYSICAL SCIENCES

Tang et al.

www.manaraa.com